A. Romei, P. Gaetani, G. Persico, *Computational fluid-dynamic investigation of a centrifugal compressor with inlet guide vanes for supercritical carbon dioxide power systems*, Energy, Vol. 255, 2022, 124469 (16 pages), doi:10.1016/j.energy.2022.124469

# Computational fluid-dynamic investigation of a centrifugal compressor with inlet guide vanes for supercritical carbon dioxide power systems

Alessandro Romei[a,*], Paolo Gaetani[a], Giacomo Persico[a]

[a]*Laboratory of Fluid Machines, Energy Department, Politecnico di Milano, Via Lambruschini 4a, Milano, 20156, Italy*

**Abstract**

A centrifugal compressor for large-scale supercritical carbon dioxide applications ($\sim 50\,\mathrm{MW}$) is analyzed by means of RANS simulations. The purposely designed compressor includes adjustable inlet guide vanes, an open impeller, and a wedge-shaped vaned diffuser. The upstream total state is located at 78.70 bar and 305.15 K, close to the thermodynamic critical point, whereby non-ideal effects and two-phase flows are significant. To account for these effects, the computational model implements a homogeneous equilibrium model (using pressure and specific enthalpy as state variables) complemented with a state-of-the-art equation of state explicit in the Helmholtz free energy and specific correlations for transport properties. It is found that the compressor can provide the entire pressure ratio required by the cycle ($\sim 3.25$) with high efficiency (87.9%, excluding parasitic losses). Three inlet vane rotations are considered: $-10\,\mathrm{deg}$, $20\,\mathrm{deg}$, and $40\,\mathrm{deg}$. The preswirl has a limited effect on efficiency, which is reduced by 0.3 percentage points away from choked conditions with vane rotation of $40\,\mathrm{deg}$. Nonetheless, the preswirl affects the extent of the two-phase region at the impeller intake, which has a detrimental impact on the compressor flexibility by setting an early choking.

*Keywords:* supercritical $CO_2$, IGV, centrifugal compressors, critical point, two-phase flows, non-ideal effects

## 1. Introduction

Closed power cycles using carbon dioxide as the working fluid are gaining interest to exploit high-temperature thermal sources, e.g., nuclear [1], concentrating solar power [2], and waste-heat recovery [3]. Leveraging the close-to-ambient critical temperature, carbon dioxide is compressed close to the critical point ($P_c = 73.77\,\mathrm{bar}$, $T_c = 304.13\,\mathrm{K}$), allowing considerable savings of the compression work thanks to the liquid-like fluid properties in

*Corresponding author

*Email address:* alessandro.romei@polimi.it (Alessandro Romei)

these thermodynamic conditions. As all state points of the thermodynamic cycle involve $CO_2$ at a supercritical state ($sCO_2$), the components benefit from a reduced size due to the large fluid density compared to advanced steam-based power cycles [4]. In addition to a reduced plant footprint, smaller equipment sizes also yield fast startups and shutdowns as well as an increased flexibility at off-design conditions [5].

One of the most critical components of $sCO_2$ power systems is the centrifugal compressor, which has to provide the required pressure ratio over an adequate flow range while operating $CO_2$ in the proximity of the critical point. The near-critical compression poses specific challenges that do not emerge in conventional compressors: (i) significant gradients in $CO_2$ thermodynamic properties, which do not allow for an ideal-gas description, [6] and (ii) possible two-phase flows due to local penetration in the saturation dome [7]. The impact of these peculiar effects on compressor operation is not yet clearly understood, pointing to the need for tailored studies in this field.

A number of works analysed these compressors with low-fidelity tools based on the mean-line description [8, 9, 10], which relies on semi-empirical correlations (calibrated mostly on air-breathing compressors) to estimate the performance. Although the mean-line model can provide realistic estimates of overall performance by incorporating basic fluid-dynamic principles, it cannot reliably account for near-critical flow features because it neglects the actual aerodynamics. Alternatively, computational-fluid-dynamics (CFD) analysis based on Reynolds-averaged Navier Stokes (RANS) offers an adequate flow representation at an acceptable computational cost. However, both non-ideal and two-phase effects require additional modeling efforts and complicate the convergence.

Operating carbon dioxide close to the critical point demands advanced equations of state (EOS) to accurately estimate thermodynamic properties. Nonetheless, adding iterative methods to evaluate thermodynamic properties aggravates the computational cost of the CFD simulation. Look-up-table (LUT) strategies alleviate this problem while preserving satisfactory accuracy in thermodynamic property estimates. The cost-effectiveness of LUT methods has already been demonstrated for the simulation of compressors operating carbon dioxide near the critical point [11, 12, 13].

Alongside non-ideal effects, the potential for the onset of two-phase flows requires particular care as well, even though the near-critical operation possibly simplifies the two-phase flow description. As a matter of fact, as the metastable region reduces close to the critical point, the two-phase mixture is expected to achieve the thermodynamic equilibrium quickly. Moreover, a relative velocity between phases is also expected to be not significant because of similar phase densities in the proximity of the critical point. Therefore, a homogeneous equilibrium model (HEM) seems appropriate to describe two-phase flows of carbon dioxide in near-critical conditions, as also suggested by past validation attempts [14, 15]. With this approach, the set of governing equations is written for the mixture along with averaged thermo-physical properties.

Many authors applied different HEM formulations to simulate compressors operating carbon dioxide close to the critical point. Pham *et al.* [16] used pressure and temperature as state variables. As pressure and temperature are not independent in the two-phase region under thermodynamic equilibrium, they smoothed thermodynamic properties across

the saturation line for numerical convergence purposes. This approximation might not alter the quality of the simulation as long as the two-phase region is limited. Ameli *et al.* [17] also used pressure and temperature as state variables but provided saturation properties as well. However, they did not discuss how mixture properties are computed using a set of dependent state variables. Hosangadi *et al.* [13] recovered thermodynamic equilibrium in an approximated manner by introducing an additional transport equation for the mass of the secondary phase and providing saturation properties as a function of the pressure. Additional computational aspects of this HEM formulation are also discussed in [9]. Finally, thermodynamically consistent HEM formulations using two independent state variables (density and internal energy) were employed by Pecnik *et al.* [11] and Shao *et al.* [18].

AMost of the above numerical studies simulated small-scale prototypes, with a particular emphasis on the one tested at the Sandia National Laboratories (SNL) [19], whose design was likely the result of a compromise between safety criteria and facility costs. As a consequence, the compressor prototype has dimensionless parameters for the work coefficient and Mach number that are not representative of technical applications. The lack of similarity conditions may prevent the identification of potential shortcomings and features that can instead characterize the operation of full-scale compressors.

To the author's best knowledge, only Saxena *et al.* [20] simulated a complete centrifugal compressor with appropriate dimensionless parameters and upstream total conditions using a thermodynamically consistent HEM formulation (density and internal energy as state variables). The compressor consisted of a closed impeller with a vaneless diffuser and included an adjustable inlet guide vane for flow regulation. They mainly focused on the effect of two-phase flows on the impeller aerodynamics without detailing the preswirl effect. Later, Persico *et al.* [21] simulated with a barotropic model the impeller and vaneless diffuser designed for the $sCO_2$-flex project, which targets a thermodynamic cycle of 25 MW. The basic HEM assumptions still apply to the barotropic model [15], but there exists a simplification in the thermodynamic property estimates. Both studies highlighted the detrimental effect of two-phase flows, which had instead a marginal role on the performance of the SNL compressor [11, 13, 17].

As previously noted, most of the research studies have focused on laboratory-scale prototypes, which might be not representative of industrial-scale compressors. Therefore, additional studies focusing on technically relevant compressors that operate $CO_2$ close to the critical point are mandatory to improve the understanding of this technology. To this end, we analyze a MW-scale compressor that includes axial inlet guide vanes (IGVs), an open impeller, and a wedge-shaped vaned diffuser. To the best of our knowledge, there are no studies related to $sCO_2$ compressors that account for all these three components simultaneously. The compressor is designed to provide the entire pressure ratio required by a 50 MW thermodynamic cycle, whose optimization also imposes realistic boundary conditions for the compressor analysis. The analysis is undertaken with a thermodynamically consistent HEM (using pressure and specific enthalpy as state variables) complemented with advanced equations for $CO_2$ properties in the form of LUTs. Based on the previous literature review, the employed computational setup represents the state of the art for the simulation of this class

of turbomachines. The compressor performance maps are derived for three inlet guide vane rotations in addition to the fully open configuration. The contributes of each component to overall performance are duly investigated by a dedicated loss analysis. Moreover, we carefully examine the IGV, which has received scarce consideration despite being important for compressor regulation. The effect of preswirl on overall compressor aerodynamics is also discussed, shedding light on its interaction with the two-phase onset.

## 2. Computational flow model

The computational model originates from the work of Smolka *et al.* [22], featuring an enthalpy-based energy equation in place of the standard energy equation based on the total enthalpy. In this way, thermodynamic equilibrium properties for the two-phase flow can be easily invoked by using pressure and static enthalpy as independent state variables. The other partial differential equations are not changed, and they are the compressible versions of continuity, momentum and, eventually, additional equations to model the effect of turbulence. Therefore, the computational model turns out to be a HEM relative to the two-phase flow description.

The model is implemented in ANSYS-Fluent®, employing the `pressure-based` solver and advecting the absolute velocity in rotating components (`absolute velocity formulation`). Steady-state conditions are assumed. The built-in energy equation is replaced with the following enthalpy-based energy equation (details about closure models in Appendix A) by means of a `user-defined scalar` (UDS):

$$\partial_i \left(\rho v_i h\right) = \partial_i \left( \left[ \frac{\kappa}{c_P} + \frac{\mu_T}{Pr_T} \right] \partial_i h \right) + v_i \, \partial_i P + \tau_{ij} \, \partial_i v_j + \rho \beta^* k \omega \tag{1}$$

where $\tau_{ij} = \mu \left( [\partial_j v_i + \partial_i v_j] - 2/3 \, \partial_k v_k \delta_{ij} \right)$. The indices follow the Einstein summation convention. $\partial_i(\cdot)$ is a shorthand for $\partial(\cdot)/\partial x_i$.

The first term on the right-hand side of equation (1) represents the diffusion of specific enthalpy, including molecular and turbulent diffusion. As illustrated by Smolka *et al.* [22], the dependency of temperature on pressure was neglected in rewriting Fourier's law, i.e. $\kappa \, \partial_i T(h,P) = \kappa (\partial T/\partial h)_P \, \partial_i h + \kappa (\partial T/\partial P)_h \, \partial_i P \approx \kappa (\partial T/\partial h)_P \, \partial_i h = \kappa/c_P \, \partial_i h$, to comply with the UDS structure requirements. This simplification is not expected to affect the quality of the results, as molecular diffusion is several orders of magnitude lower than turbulent diffusion in high-Reynolds centrifugal compressors. The turbulent diffusion includes a variable $Pr_T$ formulation as a function of $\mu_t$ and $\kappa/c_P$ [23]. The second term on the right-hand side of equation (1) is the reversible work exerted by the pressure gradient. The third term describes the irreversible degradation of mechanical energy into thermal energy. Finally, the last term represents the irreversible degradation of turbulent kinetic energy into thermal energy and is modeled on the basis of the turbulence model. The turbulence effects are included with the $k-\omega$ SST model [24], adding a rotation-curvature correction to the production terms of $k$ and $\omega$ [25].

The energy equation in (1) is invariant under transformation from the inertial frame to the rotational frame. Therefore, the same formal expression can be used in rotating

components by replacing $v_i$ with $w_i$. In analogy with Smolka *et al.* [22], the correct implementation of equation (1) is verified by simulating the impeller described in the next section with both the built-in energy equation and equation (1) while assuming ideal-gas properties. The largest discrepancy is concentrated in separated regions (e.g., wake at the trailing edge), where the specific enthalpy can differ up to a few percent. Nonetheless, as the mass-flow rate is small in separated zones, differences in integral performance parameters (e.g., efficiency) are barely measurable, i.e., below 0.1%.

The system of equations (continuity, momentum, energy, and turbulence) is solved for $[P, v_i, k, \omega, h]$ in the following way: continuity and momentum are solved in a coupled fashion, then the two turbulence equations and, finally, the enthalpy-based energy equation. After this step, thermo-physical properties ($\rho$, $\mu$, $\kappa/c_p$) are updated, and the procedure is iterated until achieving numerical (residuals below $10^{-4}$) and physical (stable torque and entropy production, mass imbalance below 0.01 kg/s) convergence. Advective terms of continuity, momentum, and enthalpy-based energy equation are discretized with the `QUICK` scheme. A `cell-to-cell` flux limiter [26] is applied to reduce spurious oscillations near discontinuities. Advective terms of turbulence equations are discretized with a `linear upwind` scheme. All diffusive terms are discretized with a second-order central differencing scheme. The gradients are computed with the `least squares cell-based` method. A `second-order` accurate method is selected to interpolate the pressure from cell centers to cell faces. The multigrid parameters are not changed from their default values.

### *2.1. Thermodynamic treatment*

Thermodynamic $(\rho, c_p)$ and transport properties $(\mu, \kappa)$ must be specified to solve the above system of equations. An accurate equation of state is necessary to correctly describe the thermodynamic properties of carbon dioxide close to the critical point. To this end, the CoolProp thermodynamic library is exploited [27]. For carbon dioxide, CoolProp implements a state-of-the-art EOS in the form of a fundamental equation explicit in the Helmhotz free energy [28] and specific correlations for transport properties [29, 30]. The choice of pressure and specific enthalpy as state variables, which motivated the formulation of the enthalpy-based energy equation in the first place, enables the calculation of the mixture density in the two-phase region, under the assumption of thermodynamic equilibrium. Therefore, the density can be estimated as follows regardless of the number of phases:

$$\rho = \mathcal{D}(P, h) \tag{2}$$

where $\mathcal{D}$ indicates the thermodynamic function made available by CoolProp that relates density with the indicated state variables.

The remaining properties $(c_p, \mu, \kappa)$ are directly evaluated via CoolProp in the single-phase region, while the volume-weighted average between the corresponding saturation properties is considered for the two-phase mixture. As an example, the formulation of $\kappa$ is explicitly reported below, with $c_p$ and $\mu$ that follow the same structure.

$$\kappa = \begin{cases} (1-\alpha_v)\mathcal{K}(P, \alpha_v = 0) + \alpha_v \mathcal{K}(P, \alpha_v = 1), & \text{if } 0 \leq \alpha_v \leq 1 \\ \mathcal{K}(P, h), & \text{otherwise} \end{cases} \tag{3}$$

with $\alpha_v = \mathcal{X}(P,h)\mathcal{D}(P,h)/\mathcal{D}(P,\alpha_v=1)$, where $y_v = \mathcal{X}(P,h)$ and $\mathcal{K}$ and $\mathcal{X}$ have the same meaning of $\mathcal{D}$ but related to $\kappa$ and $y_v$, respectively.

This way of evaluating fluid properties becomes computationally expensive when it has to be repeated at each iteration. Therefore, a LUT strategy is conceived to speed up the simulation. Following this approach, a table for each required fluid property $(\rho, \kappa/c_p, \mu)$ is built beforehand, containing discrete values of the property on a collection of grid points identified by the state variables. Missing values are obtained by a bilinear interpolation between the closest grid points. A number of `user-defined functions` (UDFs) are implemented to read the tables, store the values into arrays, interpolate the fluid properties at a generic state and, finally, provide them to the flow solver.

The LUT boundaries are set to avoid extrapolated values in the solution, and they are $P \in [20.0, 300.0]$ bar and $h \in [151, 588]\,\mathrm{kJ/kg}$, with $h_{ref} = 200\,\mathrm{kJ/kg}$ at $T = 273.15\,\mathrm{K}$ and $y_v = 0$ (saturated liquid). $1201 \times 1201$ grid points are identified by uniform steps in pressure ($0.233\,\mathrm{bar}$) and specific enthalpy ($0.364\,\mathrm{kJ/kg}$). The interpolation accuracy is assessed by looking at the error between LUTs and CoolProp values evaluated on $3603 \times 3603$ evenly spaced points. Figure 1 illustrates the relative interpolation error for the density in the thermodynamic plane $P$–$h$. The maximum relative error is 0.8% and is located across the saturation curve at low pressure and low specific enthalpy. It reduces to 0.2% across the saturation curve crossed by the isentrope $1323.70\,\mathrm{J/(kgK)}$, with $s_{ref} = 1000\,\mathrm{J/(kgK)}$ at $T = 273.15\,\mathrm{K}$ and $y_v = 0$ (saturated liquid), which corresponds to the entropy value at the compressor intake considered in this work. The maximum relative error is 0.001% in the single-phase domain and increases of two orders of magnitude in the two-phase region. Along the previous isentrope, the maximum relative error is below 0.01% in two-phase region. Similar relative errors are also found for the other properties $(\kappa/c_p, \mu)$ in the regions of interest, although the relative error of $\kappa/c_p$ steeply increase in the close proximity of the critical point ($[73.6\,\mathrm{bar}, 74.0\,\mathrm{bar}] \times [325\,\mathrm{kJ/kg}, 340\,\mathrm{kJ/kg}]$) as $c_p$ becomes singular therein.

Finally, three additional tables are generated for temperature, specific entropy, and vapor mass fraction (at thermodynamic equilibrium), respectively, employing the same range and discretization steps in pressure and specific enthalpy. These three quantities are invoked at the end of the simulation only for post-processing purposes.

As a final comment, employing thermodynamic properties tabulated as a function of pressure and specific enthalpy is expected to be advantageous for numerical stability. Many CFD software implement LUT approaches based on pressure and temperature as state variables. Besides preventing a straightforward application of the HEM for two-phase flows, this latter choice also complicates the convergence for single-phase flows near the critical point. Actually, if the specific enthalpy is the independent variable of the energy equation in the pressure-based solver, it should be converted to temperature before interrogating LUTs to evaluate fluid properties. This conversion may compromise the stability of the simulation because it involves the specific heat at constant pressure, which diverges at the critical point. On the contrary, in the present computational strategy, the specific heat at constant pressure appears only in the diffusion term of the enthalpy-based energy equation, see equation (1). As the enthalpy diffusion coefficient is $\kappa/c_P$, possible large $c_P$ values close to the critical point are not perilous for numerical stability because the molecular diffusion term

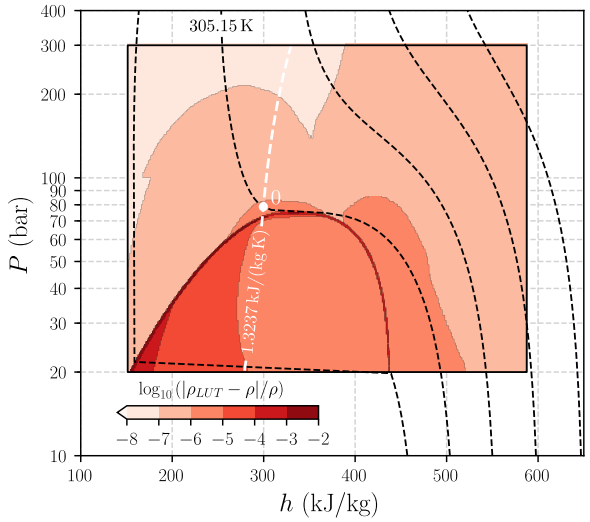


Figure 1: Relative interpolation error between $(1201 \times 1201)$–LUT interpolated values ($\rho_{LUT}$) and CoolProp values ($\rho$) on $3603 \times 3603$ evenly spaced grid points. The state 0 indicates the total state upstream of the compressor, and the dashed white line is the corresponding isentrope. Black dashed lines are isoterms with a constant step of 50 K.

harmlessly tends to zero when $c_P$ approaches infinity. Lastly, the effect of $c_P$ on turbulent diffusion depends on the $Pr_T$ formulation; in this work (see Appendix A), $Pr_T$ approaches the free-stream value of 0.85 when $c_P$ tends to infinity.

### *2.2. Validation*

The computational model is validated against experiments performed by Nakagawa *et al.* [31]. They measured pressure and temperature along several axial locations of converging-diverging nozzles, which expand $CO_2$ from single-phase states to two-phase conditions, according to the considered flashing process. To validate the computational model, we consider the experimental data related to the supercritical expansion ($P = 91$ bar, $T = 310.45$ K), which is most representative of operating conditions of interest for $sCO_2$ power cycles.

The governing equations and the thermodynamic tables are discretized as described in previous sections. The total state is prescribed at the inlet section, in which the hydraulic diameter (10 mm) and the eddy viscosity ratio (2.5) are also specified for the turbulent equations. A static pressure equal to 27.5 bar is provided at the outlet boundary. Adiabatic and no-slip conditions are assigned to the wall, while the symmetry condition is exploited at the nozzle axis. Due to the small-scale of the experiment coupled with the high Reynolds number, the roughness is expected to be significant and an equivalent sand-grain roughness equal to 6.2 µm is specified at the solid wall [15].

The computational domain and the mesh are reported in figure 2 (top) with main nozzle dimensions. The first-layer center cell distance is dictated by the roughness value, yielding nine evenly spaced elements along the nozzle height. The resolution along the x-direction increases in the converging section, reaching a value of $2 \times 10^{-5}$ m at the throat, which is

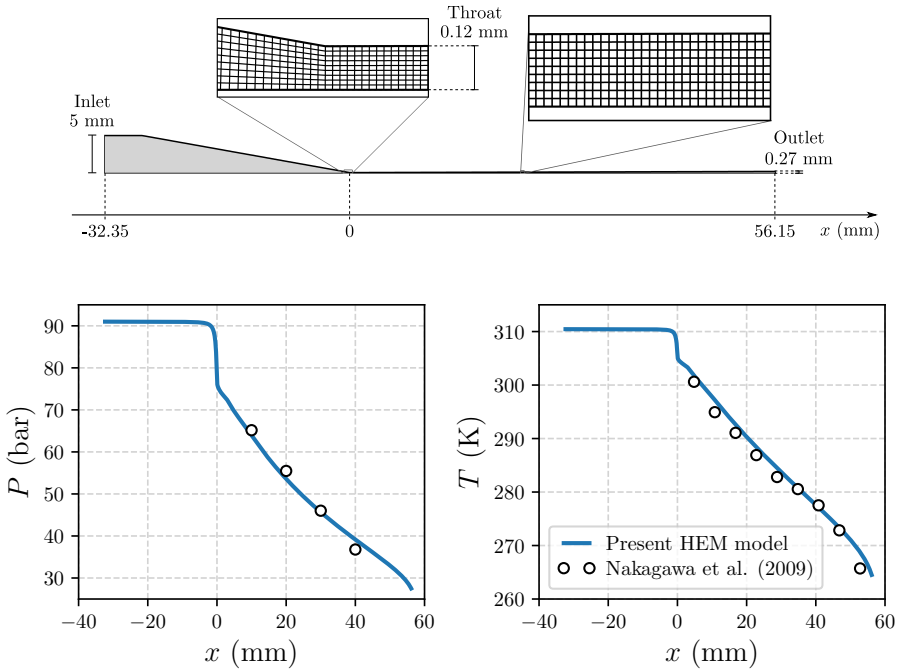


Figure 2: Validation of the HEM against experimental data of a flashing $CO_2$ flow near the critical point [31].

maintained in the diverging section. A grid convergence assessment halving and doubling the element counts shows no quantifiable variations in the main trends in analogy to what reported in our previous work [15].

The evolution of pressure and temperature along the nozzle axis predicted by the computational model are compared against experiments in figure 2. The computational trends correctly reproduce the ones determined by the experimental data, which are all taken in the two-phase flow region. The maximum relative error is 6.4% and 1.1% for the pressure and temperature, respectively, both located at the last measurement site.

Notwithstanding the excellent agreement between experiments and computations in predicting flashing flows of $CO_2$ in near-critical conditions, one might argue to what extent such agreement applies to cavitating flows in industrial-scale $sCO_2$ compressors. Very recently, Toni *et al.* [32] experimentally tested a 5 MW centrifugal compressor in the frame of $sCO_2$-flex project complying with the ASME PTC-10 Type I code, i.e., the compressor was operated under design conditions in terms of fluid composition, upstream total state, and operating conditions. It was found that a CFD simulation model based on homogeneous equilibrium proficiently predicts the compressor characteristic curve, thus assuring technical relevance to the computational model here adopted.

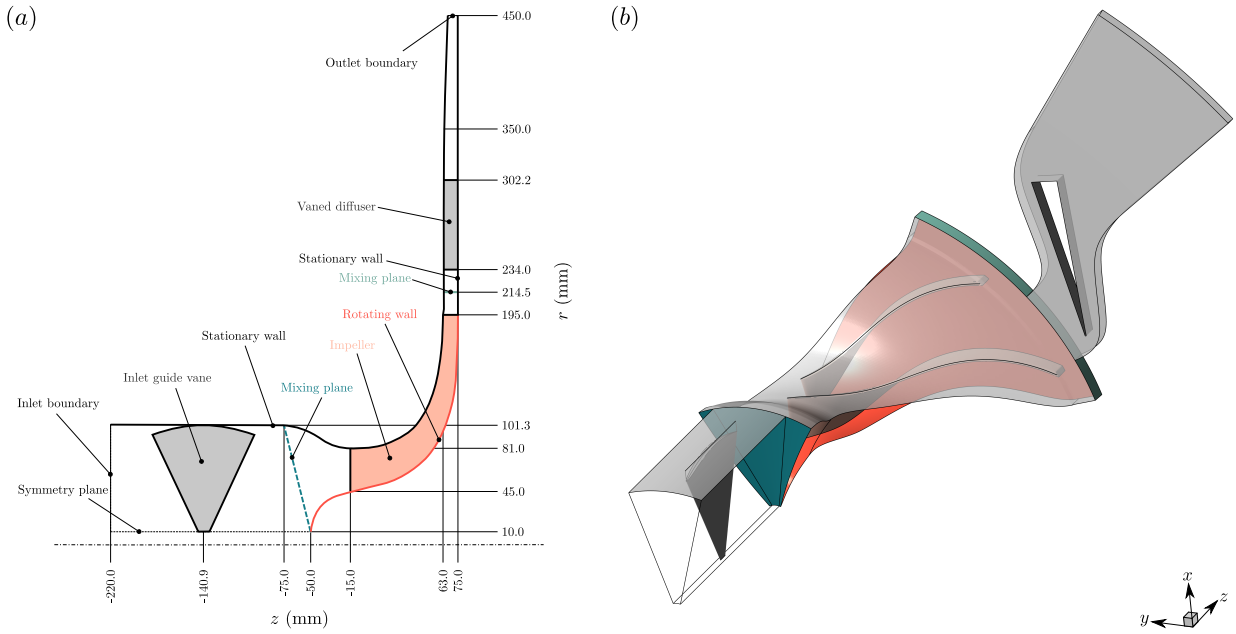


Figure 3: Meridional ($a$) and three-dimensional ($b$) view of the centrifugal compressor with the geometrical dimensions of the meridional shape.

## 3. Centrifugal compressor geometry

The centrifugal compressor under study is representative of a single-stage main compressor for closed $sCO_2$ power cycles. Realistic requirements are derived from a dedicated optimization of the thermodynamic cycle with a target power of 50 MW. The main cycle assumptions and the optimization procedure can be found in Romei *et al.* [9]. As a result, the best-efficiency cycle requires the compressor to provide an overall pressure ratio of 3.25, while elaborating $\dot{m}_d = 413.4\,\mathrm{kg/s}$. The intake thermodynamic state is $P_0 = 78.70\,\mathrm{bar}$ and $T_0 = 305.15\,\mathrm{K}$, it is supercritical and lies in the liquid-like domain ($s < s_c$).

The centrifugal compressor simulated in this work includes an axial IGV, an open impeller with inducer, and a wedge-shaped vaned diffuser. In the conditions of interest, single-phase $CO_2$ behaves like a compressible liquid and is not affected by the peculiar density gradients typical of operation across the pseudo-critical line. Therefore, each component has been designed in accordance with well-consolidated design principles. A preliminary design determining main geometrical parameters is obtained by mean-line optimization [9]. For specific information about the aerodynamic design, the reader is referred to dedicated textbooks, e.g. [33, 34]. The resulting meridional shape with main dimensions is illustrated in figure 3$a$. Additional geometrical parameters are listed in table 1. Figure 3$b$ shows the three-dimensional layout.

The IGV is made of a symmetric NACA profile with constant solidity along the span. The tip profile assumes a spherical shape to enable vane rotation (the struct is omitted). The cross-section is enlarged to reduce the velocity and, hence, fluid-dynamic losses. As an additional benefit of the enlarged cross-section, the low momentum flow downstream of the

Table 1: Main geometrical parameters. Blade angles are measured from the meridional coordinate (positive in the direction of the rotation).

| **Inlet guide vane** | | **Impeller** | LE | TE | **Vaned diffuser** | |
|---|---|---|---|---|---|---|
| Vanes | 11 | Main blades | 7 | | Vanes | 23 |
| Solidity | 1.5 | Splitter blades | 7 | | Vane height (mm) | 11.1 |
| Minimum clearance (mm) | 0.1 | Blade height (mm) | 35.5 | 11.5 | Inlet vane angle (deg) | 69.0 |
| Thickness distribution | NACA0015 | Tip clearance (mm) | 0.5 | | Vane length (mm) | 125.0 |
| | | Blade angle hub (deg) | -48.4 | -45.0 | Inlet vane blockage | 0.04 |
| | | Blade angle shroud (deg) | -60.2 | -45.0 | Divergence angle (deg) | 4.5 |
| | | Blade blockage | 0.06 | 0.02 | Area ratio | 2.49 |

tip clearance is accelerated through the decreasing area passage.

The inlet section of the impeller is designed by minimizing the relative Mach number at the tip coordinate and by including structural considerations for a feasible hub diameter. Splitter blades are exploited to reduce the blade blockage at the entrance while providing adequate flow guidance on the aft part of the blade, where most of the flow deflection occurs. In fact, an aft-loading blade angle distribution is devised to minimize the flow acceleration on the front part of the blade, which can promote two-phase flows due to the vicinity of the intake thermodynamic state to the saturation curve. Finally, the selection of backward blades prevents an excessive swirl component at the impeller outlet, which can limit the compressor flow range. The resulting impeller has a flow coefficient of $\phi_d = 0.021$ at design conditions. As both the rotational speed ($\omega = 1047.2\,\mathrm{rad/s}$) and the intake total state ($P_0 = 78.70\,\mathrm{bar}$, $T_0 = 305.15\,\mathrm{K}$) are fixed, the Mach number and Reynolds number based on the peripheral velocity ($M_{u2}$, $Re_{u2}$) do not change as well and are 0.86 and $3.1 \times 10^7$, respectively.

A pinch follows just downstream of the impeller, decreasing the flow-passage height by 7.5%. The diffuser channel design leverages the extensive databases available in the literature [33], and the main geometrical parameters are selected to maximize the pressure recovery coefficient.

### *3.1. Boundary conditions*

Total pressure ($P_0 = 78.70\,\mathrm{bar}$) and total enthalpy ($h_0 = 299\,608.256\,\mathrm{J/kg}$) are prescribed at the inlet boundary (upstream of the IGV) alongside the axial flow direction. As the enthalpy-based energy equation asks for boundary conditions in terms of static enthalpies, a UDF converts the total enthalpy into static enthalpy depending on the local kinetic energy. A turbulence intensity of 1% and an eddy-viscosity ratio equal to 1 (representative of a low turbulence level) are also prescribed. Note that preliminary calculations showed a negligible contribution of the intake turbulence level on the compressor performance.

The stationary and the rotating domains are connected via a mixing-plane interface, in which main flow quantities are mass-flow averaged over the circumferential direction and passed as boundary conditions to the adjacent components. Mixing plane interfaces (between IGV-impeller and impeller-diffuser) are shown in figure 3. In this way, a single-blade passage with periodic boundary conditions is simulated for each component. The averages

are corrected to preserve the mass-flow rate across the interface by selecting `mass flow inlet` boundary conditions for the downstream components. The mixing plane capabilities are extended for the enthalpy-based energy equation by developing a UDF that mass-flow averages the total enthalpy across the upstream interface and, then, provides the averaged value to the downstream interface. The total enthalpy is ultimately converted into static enthalpy similarly to the inlet boundary condition.

No-slip and adiabatic (zero enthalpy flux) boundary conditions are imposed at the wall boundaries. Due to the comparatively large Reynolds number, the viscous sublayer is estimated to be smaller than the roughness level, which is introduced in terms of sand-grain roughness equal to 5 µm for both blades and endwalls. All walls are stationary except for the main and splitter blades of the impeller and the associated hub surface. A symmetry boundary condition (zero fluxes) is placed at $r = 10.0$ mm where IGV stops.

The outlet boundary is placed at $r = 450.0$ mm and is preceded by a converging section that starts at $r = 350.0$ mm and reduces the channel height by 25%. This converging section helps suppress possible reverse flows at the outlet boundary. For each IGV opening, the design condition $\phi = \phi_d$ is first simulated by assigning the design mass flow rate. Then, either the mass flow rate ($\phi < \phi_d$) or the static pressure ($\phi > \phi_d$) is specified depending on the flow coefficient. For $\phi < \phi_d$ (towards surge), the mass flow rate is progressively reduced by 5% from the design value until flow separation prevents achieving a steady solution. For $\phi > \phi_d$ (towards choking), the static pressure is progressively reduced by $\sim 3.5$ bar from the design value until the mass-flow rate does not vary anymore. Finally, zero flux of static enthalpy is prescribed in all cases.

### *3.2. Grid analysis*

The spatial discretization error is estimated via the grid convergence index (GCI) method based on the Richardson extrapolation. To this end, three structured grids with an increasing number of elements are generated with ANSYS Turbogrid®. The medium grid (grid 2) has 3 185 740 elements, of which 620 840 for the IGV, 1 971 216 for the impeller, and 593 684 for the vaned diffuser. Between 10 and 15 elements are placed near walls with a first-layer distance of the same order of the sand-grain roughness ($5 \times 10^{-6}$ m) and an expansion ratio in the range of $1.2 - 1.4$. 20 layers are placed in tip clearances. The blade-to-blade planes contain about 15 000 (IGV), 30 000 (impeller), and 25 000 (vaned diffuser) elements, and the pitch is discretized with 34, 56, and 49 cells, respectively. A finer (grid 1) and coarser (grid 3) mesh are generated with double and half elements relative to the medium grid, respectively, without altering the layer distributions at the walls and within the clearances.

Known the values of key variables $x^{(i)}$ obtained with the three meshes (with $i = 1, 2, 3$ referring to the corresponding computational grid), then the apparent order $p$ of the method, the extrapolated value $x_{ext}$, the approximate $e_a$ and extrapolated $e_{ext}$ relative errors, and the GCIs can be evaluated [35]. The key variables to assess the discretization error are the total-total isentropic efficiency, the work coefficient, and the total-total pressure ratio, and

Table 2: Outcomes of the grid analysis.

| $x =$ | $\eta$ | $\Pi$ | $\lambda$ |
|---|---|---|---|
| $x^{(1)}$ | 0.8825 | 3.268 | 0.6780 |
| $x^{(2)}$ | 0.8790 | 3.257 | 0.6775 |
| $x^{(3)}$ | 0.8735 | 3.236 | 0.6758 |
| $p$ | 1.96 | 2.86 | 5.28 |
| $x_{ext}$ | 0.8885 | 3.278 | 0.6777 |
| $e_a$ | 0.39% | 0.34% | 0.07% |
| $e_{ext}$ | 1.07% | 0.69% | 0.10% |
| **GCI** | 1.35% | 0.87% | 0.13% |

they are defined, respectively, as:

$$\eta = \frac{l_{is}}{l} = \frac{\mathcal{H}(P_{\hat{3}}^t, s_0) - h_0^t}{h_{\hat{3}}^t - h_0^t} \tag{4a}$$

$$\Pi = \frac{P_{\hat{3}}^t}{P_0^t} = \frac{\mathcal{P}(h_{\hat{3}}^t, s_3)}{P_0^t} \tag{4b}$$

$$\lambda = \frac{l}{u_2^2} = \frac{h_{\hat{3}}^t - h_0^t}{u_2^2} \tag{4c}$$

where $\mathcal{H}$ and $\mathcal{P}$ are thermodynamic functions that relate specific enthalpy and pressure, respectively, with the indicated state variables. Consistently with the CFD thermodynamic model, $\mathcal{H}$ and $\mathcal{P}$ are evaluated via the CoolProp library. State 0 indicates the stagnation state at the compressor intake, state $\hat{3}$ refers to the mixed-out state computed from section $r = 317.3\,\text{mm}$. Appendix B details how to compute the mixed-out state in the context of an arbitrary thermodynamic model.

All results obtained from this grid assessment are duly reported in table 2, including the GCI for the medium-grid solution. The maximum GCI is found for the efficiency, amounting to 1.35% ($0.8790 \pm 0.0119$). The discretization error for the pressure ratio is 0.87% ($3.257 \pm 0.028$), while a comparably smaller error affects the estimate of the work coefficient, namely 0.13% ($0.6775 \pm 0.0009$). The fine-grid GCI obviously reduces compared to its medium-grid counterpart, and it is 0.86%, 0.45%, and 0.04% for efficiency, pressure ratio, and work coefficient, respectively.

Alongside the discretization error, the computational cost is also a decision variable. A single simulation with the medium grid requires approximately one and a half days to converge on a cluster node "Dell Intel® Xeon® Gold 6148" equipped with 40 cores. The need for significant under-relaxations considerably contributes to this computational cost by increasing the number of iterations to achieve convergence. The computational cost scales roughly linearly with the number of elements. Therefore, the medium grid displayed in figure 4 is selected as a trade-off between accuracy and computational cost.

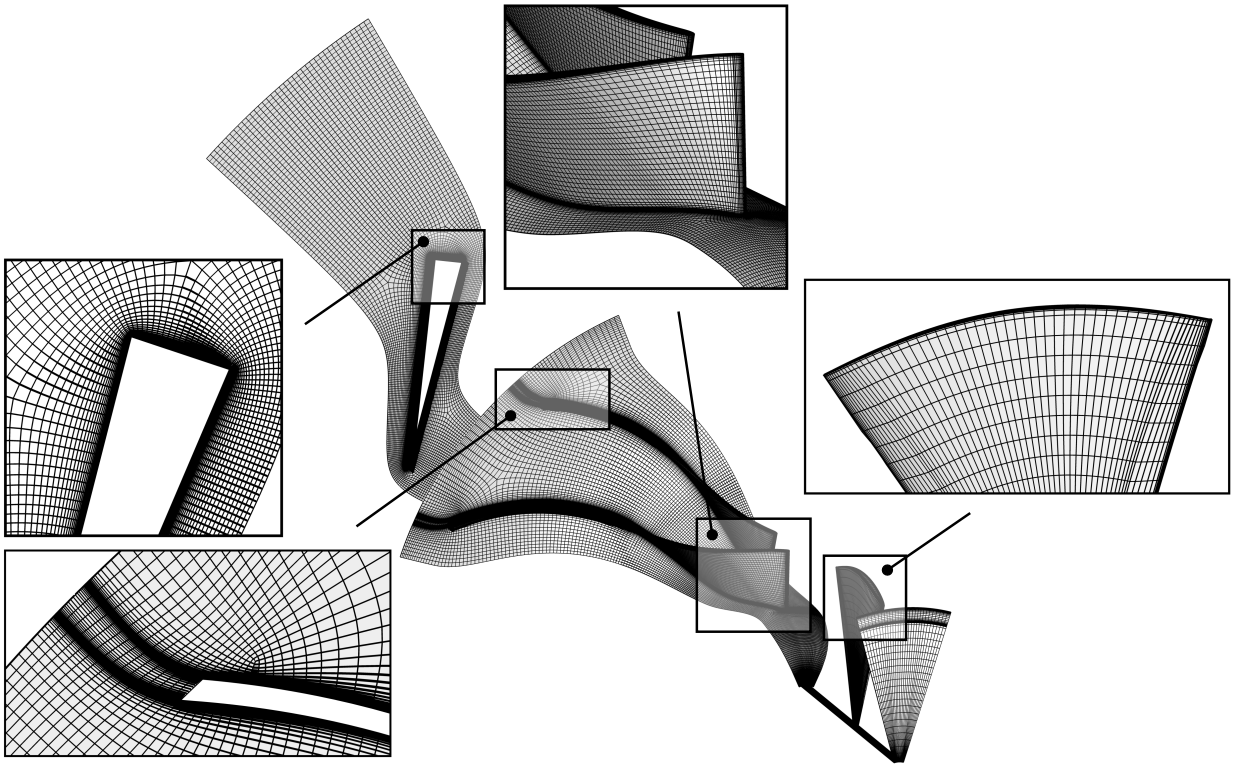

Figure 4: Reference mesh for subsequent calculations with zooms in the most critical regions (sharp edge and large curvature regions).

## 4. Compressor performance

Three IGV rotations are simulated in addition to fully open condition. With reference to the nomenclature in figure 5, one negative rotation ($-10\,\text{deg}$) and two positive rotations ($20\,\text{deg}$, $40\,\text{deg}$) are considered. The computational domain for the IGV is regenerated at each vane rotation without altering the cell distribution discussed in section 3.2. The vane rotation induces a swirl component in the flow upstream of the impeller (equivalently called prerotation or preswirl) as illustrated by velocity triangles in figure 5. A negative prerotation adjusts the impeller incidence angle at large flow rates and increases both the relative Mach number and the eulerian work compared to fully open condition. The opposite occurs for a positive preswirl.

The performance maps for different IGV rotations are reported in figure 6. They are expressed in terms of the key quantities introduced in equations (4) as a function of the normalized flow coefficient.

On the one hand, the left limit of the curve is at $\phi/\phi_d = 0.90$ regardless of the IGV rotation. As previously mentioned, this limit is imposed by the non-existence of a steady solution (periodic oscillations of main quantities, e.g., torque and outlet pressure), which does not necessarily identify the onset of surge. Moreover, we observed a decrease in the

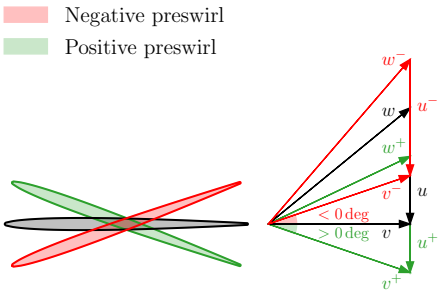


Figure 5: Effect of preswirl on velocity triangles at the impeller inlet.

average totalstatic pressure rise for $\phi/\phi_d < 0.9$, which represents a further indication of near-stall operation [36]. As these periodic oscillations in the solution are nearly independent of the amount of preswirl, the presence of possible time-dependent phenomena needs to be located outside the impeller. An inspection of the flow fields reveals that the stall originates from the diffuser suction side, which ultimately prevents achieving a steady solution for $\phi/\phi_d < 0.90$.

On the other hand, the right limit of the curve (choking limit) changes with the preswirl, from $\phi/\phi_d = 0.95$ with 40 deg of preswirl to $\phi/\phi_d = 1.10$ with $-10$ deg of preswirl. As the choking is linked with the onset of the secondary phase, this analysis is postponed to section 5 that specifically focuses on two-phase effects.

The preswirl induces a tangential component in the absolute velocity, hence the work coefficient changes in accordance with the Euler equation, i.e., it increases for negative preswirl and decreases otherwise. The same occurs for the pressure ratio, because the peripheral Mach number and the upstream total state are fixed and the efficiency slightly changes. The pressure ratio at design condition is $\Pi_d = 3.26$ ($\pm 0.03$ considering the discretization error), which meets the cycle requirement declared in section 3.

The efficiency at design condition is $\eta_d = 87.9\%$ ($\pm 1.2\%$ considering the discretization error). Such a high value is justified by the large scale of the machine that complies with the nominal power of the cycle, which reduces the importance of non-scalable geometrical parameters (e.g., clearance and roughness), and by the high Reynolds number, which reduces turbulent dissipation. Note that the efficiency here reported only considers the aerodynamic losses (sometimes referred to as *internal losses*). The overall efficiency has also to account for parasitic losses, such as disk friction and leakages through seals (sometimes referred to as *external losses*). Finally, the efficiency is marginally affected by prerotation up to 20 deg in the range $0.90 \leq \phi/\phi_d \leq 1.00$. For $\phi > \phi_d$, compressible effects related to choking make efficiency curves depart. A reduction in efficiency is instead observed for preswirl 40 deg. A dedicated loss analysis is presented in the next section to highlight the role of each component to efficiency variations.

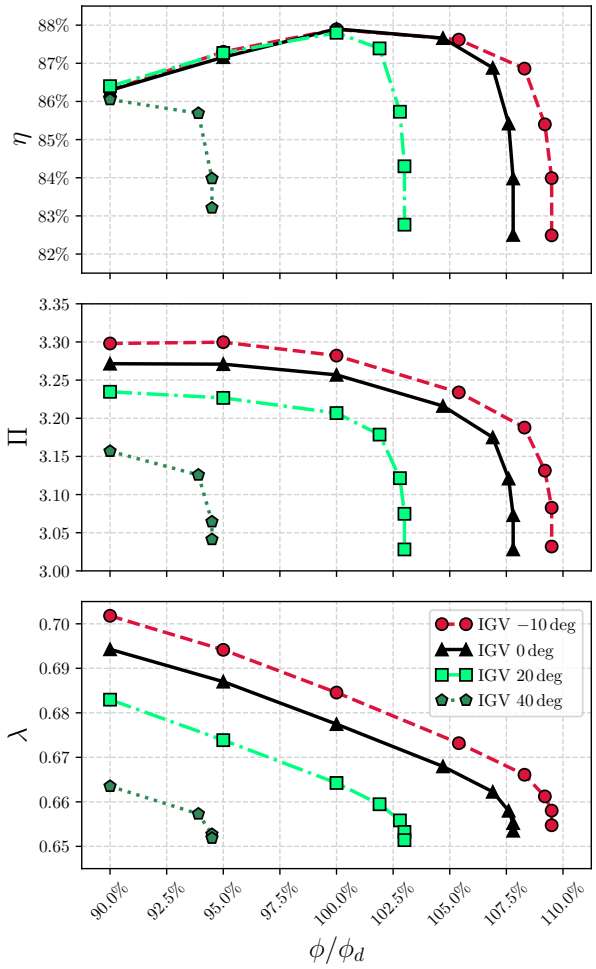


Figure 6: Performance maps in terms of total-total efficiency, total-total pressure ratio, and work coefficient for different IGV rotations.

### *4.1. Loss decomposition*

The total-total efficiency reported in equation (4a) is rewritten to highlight the separate shares of IGV ($\Delta\eta_i$), impeller ($\Delta\eta_r$), and vaned diffuser ($\Delta\eta_d$) loss:

$$\eta = 1 - \underbrace{\frac{h_{\hat{3}}^t - \mathcal{H}(P_{\hat{3}}^t, s_{\hat{2}})}{h_{\hat{3}}^t - h_0^t}}_{\Delta\eta_d} - \underbrace{\frac{\mathcal{H}(P_{\hat{3}}^t, s_{\hat{2}}) - \mathcal{H}(P_{\hat{3}}^t, s_{\hat{1}})}{h_{\hat{3}}^t - h_0^t}}_{\Delta\eta_r} - \underbrace{\frac{\mathcal{H}(P_{\hat{3}}^t, s_{\hat{1}}) - \mathcal{H}(P_{\hat{3}}^t, s_0)}{h_{\hat{3}}^t - h_0^t}}_{\Delta\eta_i} \tag{5}$$

where $\hat{1}$, $\hat{2}$, and $\hat{3}$ are the mixed-out states computed from sections $z = -75.0\,\text{mm}$ (downstream of the IGV), $r = 214.0\,\text{mm}$ (downstream of the impeller), and $r = 317.3\,\text{mm}$ (downstream of the vaned diffuser), respectively. Since $s_{\hat{1}}$ varies along the radius to comply with radial equilibrium (see Appendix B), the corresponding radial-averaged value is considered for the loss evaluation. As the second mixed-out location is halfway between the impeller

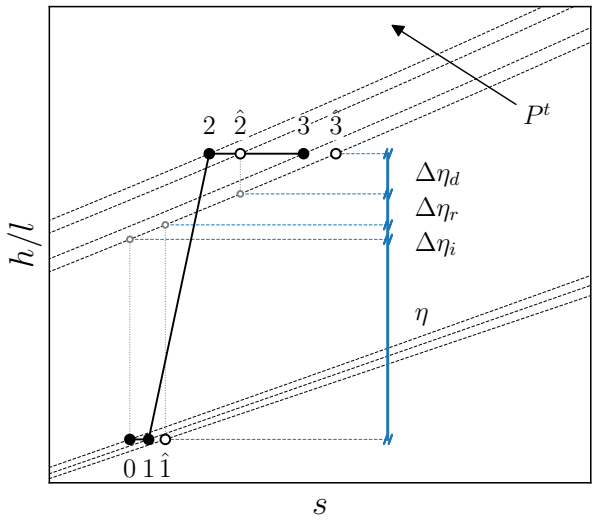


Figure 7: Graphical interpretation of the component loss definition in equation (5), including the representation of mixed-out states.

and the vaned diffuser, the entropy generated in the vaneless space is included in the performance of the two latter components. For the sake of interpretability, Figure 7 provides a graphical representation of losses defined in equation (5) on the Mollier diagram. This figure also offers the chance to highlight the difference between the measured state and the corresponding mixed-out state, whereby an extra entropy production due to mixing is attributed to the component that generates the non-uniform flow in the first place. Finally, it is worth recalling that the enthalpy increase at constant pressure can be equivalently treated as irreversible entropy production in adiabatic components, i.e., $dh = Tds + dP/\rho$ with $dP = 0$.

Figure 8 illustrates the share of each component loss. For IGV rotation smaller than 40 deg, the loss associated with the IGV is negligible (maximum 0.2% for 20 deg of preswirl, less than 0.1% in the remaining conditions). The highest loss is produced by the vaned diffuser: it amounts to 7.5% at $\phi = \phi_d$ and increases departing from the design flow coefficient. Additionally, the loss produced by the impeller is 4.5% at $\phi = \phi_d$ and remains approximately constant at lower flow rates (variations within $\pm 0.2\%$). Both impeller and vaned diffuser loss are nearly independent of the initial preswirl (variations within $\pm 0.4\%$).

Losses with 40 deg of preswirl are barely comparable with the other cases, as all simulated flow conditions are close to choking, and losses are affected by associated compressible effects. However, the IGV precedes the sonic throat, therefore the corresponding losses are generated by flow separation due to incidence rather than choking-related effects. In this case, the overall loss produced by the IGV becomes relevant and amounts to 1.0% across the whole flow range.

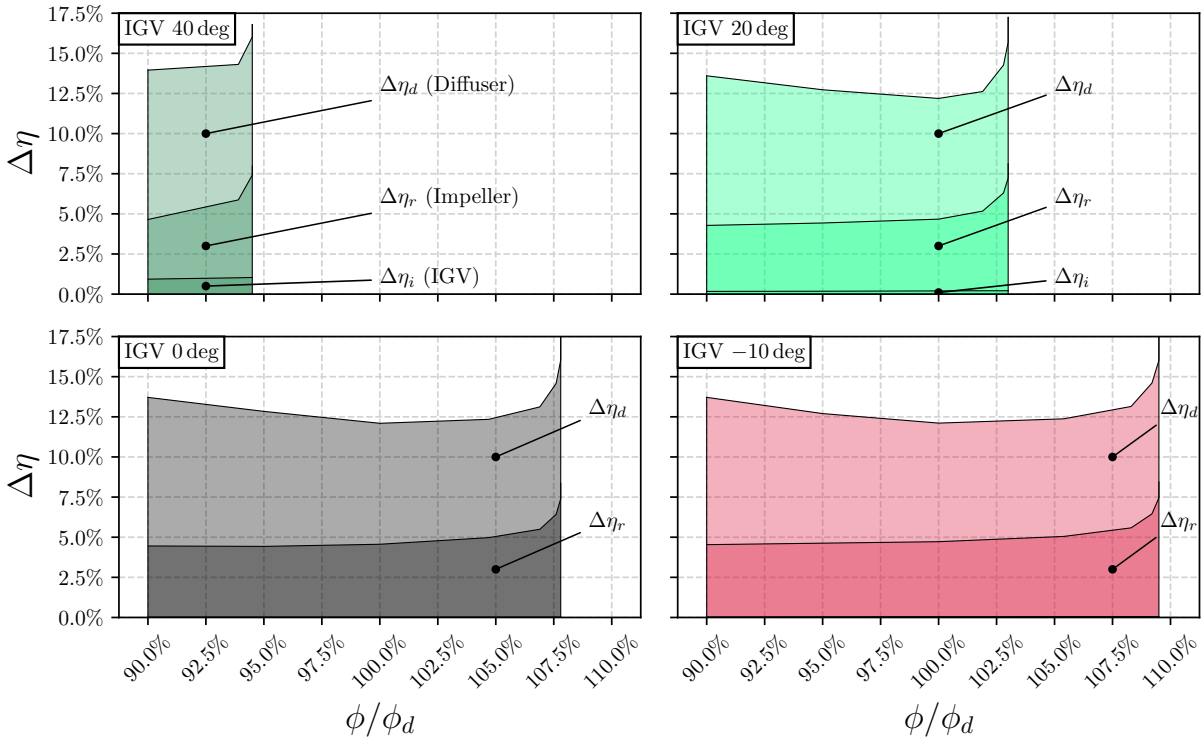


Figure 8: Loss decomposition for different IGV rotations.

*4.2. Aerodynamic analysis*

Until now, the discussion has focused on integral parameters. Next, local phenomena that contribute to the overall efficiency are examined. At first, the case with zero preswirl is analyzed in figure 9, in which the local dissipation $T(s - s_0)$ normalized to the eulerian work is displayed at midspan. Besides the design flow rate, dissipation fields are also reported for the minimum flow rate ($\phi/\phi_d = 0.90$) and the choking flow rate ($\phi/\phi_d = 1.08$).

The major dissipation in the impeller is provided by a flow separation on the suction side, which generates local irreversibilities up to 10%. The amount of this dissipation is nearly constant between $0.90\,\phi_d$ and $\phi_d$, consistently with the flat trend of the impeller loss discussed in figure 8. Then, the relative weight of this separation locally increases up to 20% for $1.08\,\phi_d$ (labelled as 'C' in figure 9*c*). The larger dissipation is promoted by the shock (labelled as 'B' in figure 9*c*) that onsets on the front part of the impeller. Moreover, the shock also produces by itself a net increase in entropy production (+4%). Another significant source of loss for the impeller is the tip clearance (here not reported), but it displays a trend with the flow rate comparable with the separation loss. Finally, the incidence loss is hardly quantifiable (less than 1%) in all three flow conditions.

The wake downstream of the trailing edge is the major source of loss for the vaned diffuser (about 15-18%). The dissipation field is qualitatively similar for $\phi_d$ and $1.08\,\phi_d$, differing only for the larger level of dissipation in the latter case. By looking at figure 9*a*,

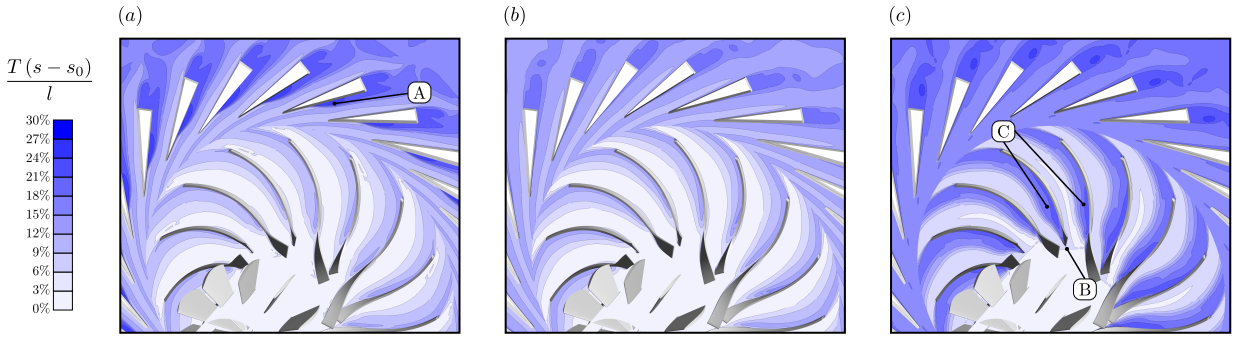


Figure 9: Dissipation fields at midspan for (*a*) $\phi/\phi_d = 0.90$, (*b*) $\phi/\phi_d = 1.00$, and (c) $\phi/\phi_d = 1.08$ (choking) with zero preswirl.

a significant separation occurs on the vane suction side (labelled as 'A' in figure 9*a*), which is responsible for the largest level of dissipation (around 20%). Moreover, this separation is reputed to be the cause that prevents a steady convergence for flow rates $\phi/\phi_d < 0.90$.

As previously discussed, the preswirl slightly affects the integral loss of the impeller and vaned diffuser. In fact, similar fields of local dissipation with the flow rate are also observed at different preswirls and, hence, are not explicitly reported here. On the contrary, it is interesting to investigate the dissipation produced by the IGV at various vane rotations. To this end, figure 10 illustrates the normalized local dissipation (defined as before) on a secondary plane placed at $z = -75\,\mathrm{mm}$ for $\phi/\phi_d = 0.90$. As the dissipation produced by the IGV is small compared to the overall, the step of isolevels is reduced compared to figure 9 (from 3.0% to 0.1%). The only source of dissipation at 0 deg and $-10$ deg of preswirl are given by the wake and the tip clearance. However, the corresponding losses are localized and quantitatively negligible ($< 0.2\%$). Increasing the vane rotation to 20 deg, the flow separates and tends to accumulate near the hub region because of the radial pressure gradient [34]. Moreover, the extent of the tip clearance loss also increases due to the larger pressure unbalance between vane pressure and suction side. The last case for vane rotation of 40 deg exhibits a trend similar to the case at 20 deg, but quantitatively more significant. The separated flow occupies almost half of the span and the corresponding loss amounts to $\sim 1\%$. The tip clearance loss is also more significant, producing 0.4% of dissipation over approximately 70% of the pitch.

All losses mechanisms have been discussed in terms of consolidated fluid-dynamic principles, and peculiar effects related to the non-ideal thermodynamics of $CO_2$ close to the critical point do not emerge. Nonetheless, unconventional phenomena related to two-phase flows do take place, and they are thoroughly examined in the next section.

## 5. Two-phase effects

As the upstream total state is close to the critical point, flow acceleration can drive the local thermodynamic state inside the saturation dome, originating two-phase flows. The extent of the two-phase region is affected by several factors, among them (i) initial

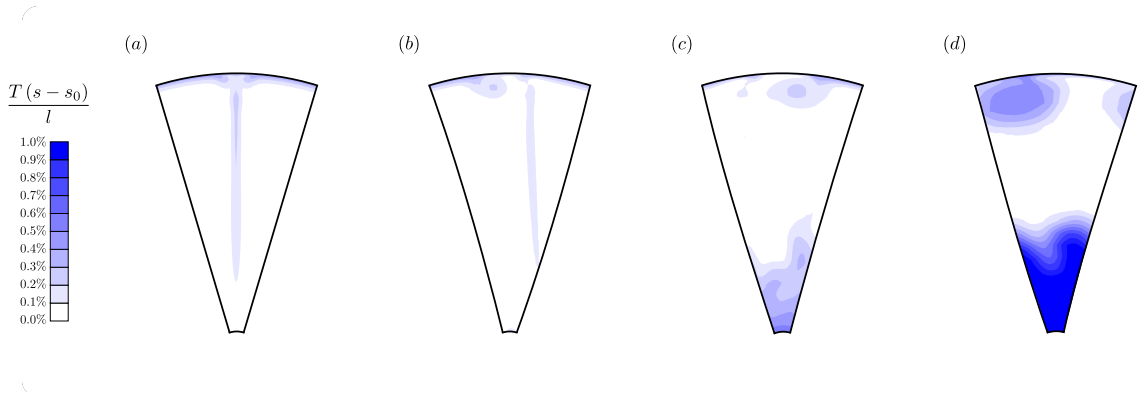


Figure 10: Dissipation fields downstream of the IGV for $\phi/\phi_d = 0.90$ with $(a)$ 0 deg, $(b)$ $-10$ deg, $(c)$ 20 deg, and $(d)$ 40 deg of preswirl.

thermodynamic state, determining the margin from the saturation condition, (ii) Mach number, as a measure of the flow velocity, (iii) blade loading, affecting local flow acceleration, (iv) flow incidence, prompting a flow turning towards the blade angle direction, and (v) blade blockage, inducing a flow acceleration due to the reduction in the passage area.

The following discussion on two-phase flows focuses on both the IGV and the effect of the associated preswirl on the successive impeller. The IGV operates as close to the critical point as the impeller, it accelerates the fluid, and, above that, there can be local acceleration on the blade surface that can theoretically trigger two-phase flows. As the upstream state lies in the liquid-like domain ($s < s_c$), the entropy production across the IGV reduces the margin of the impeller from saturation. Besides, the preswirl can modify the incidence and affects the inlet Mach number (see velocity triangles in figure 5) and the blade loading distribution (because of the change in the work coefficient).

Figure 11 shows the extent of the two-phase region, intended as the isosurface of vapor mass fractions $y_v = 0.001$, for different vane rotations at $\phi/\phi_d = 0.90$. As stated in section 2.1, the vapor mass fraction can be directly evaluated through the pair pressure and specific enthalpy using the corresponding LUT. The figure shows that the secondary phase appears mainly in the front part of the impeller blade. A limited region is also visible on the IGV suction side when it is rotated by 40 deg. The rear impeller blades and the diffuser vanes are cavitation-free. The extent of the two-phase region is larger at positive prerotation (negative incidence), despite the lower relative Mach number and work coefficient. Therefore, the mismatch between blade and flow angle is mainly responsible for this variation. Besides localized effects in the neighborhood of the stagnation point, the relative flow angle is more axial than the blade angle by increasing the preswirl at fixed flow rate. Hence, the flow accelerates in turning towards the blade direction. On the contrary, the extent of the two-phase region remains nearly constant passing from 0 deg to $-10$ deg of preswirl. It is worth recalling that the entropy increase across the IGV is not negligible for a preswirl of 40 deg, hence the larger vapor fraction in this condition can be also a consequence of a reduced margin from saturation at the impeller intake.

To have a quantitative estimate of the amount of phase change, the integral vapor mass

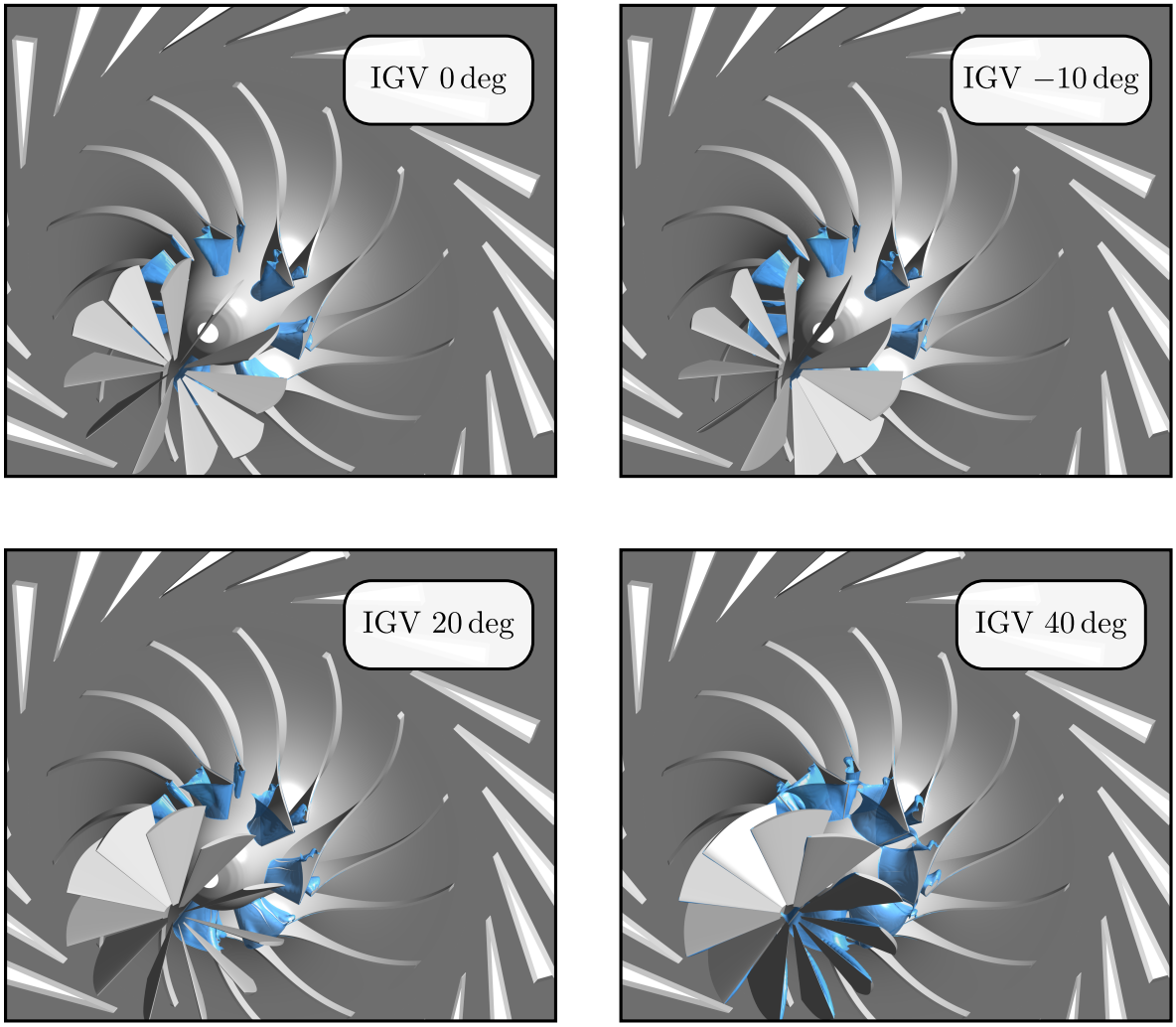


Figure 11: Extent of the two-phase flow region for $\phi/\phi_d = 0.90$ with different preswirls.

fraction is computed in each component domain as:

$$\varsigma_v = \frac{\int \alpha_v \rho_v \, dV}{\int \rho \, dV} \tag{6}$$

The results are reported in Figure 12 for the IGV and the impeller. The vaned diffuser is always cavitation free. As previously noted in a qualitative way, the IGV does feature two-phase flows at vane rotation 40 deg, albeit localized and quantitatively small ($\varsigma_v < 0.10\%$). The largest share of vapor phase is found in the impeller. The vapor mass fraction increases with the flow rate because of the relative increase in flow velocity to process the higher flow rate. $\varsigma_v$ is limited far from choking ($< 1\%$) but steeply increases up to 4% by approaching

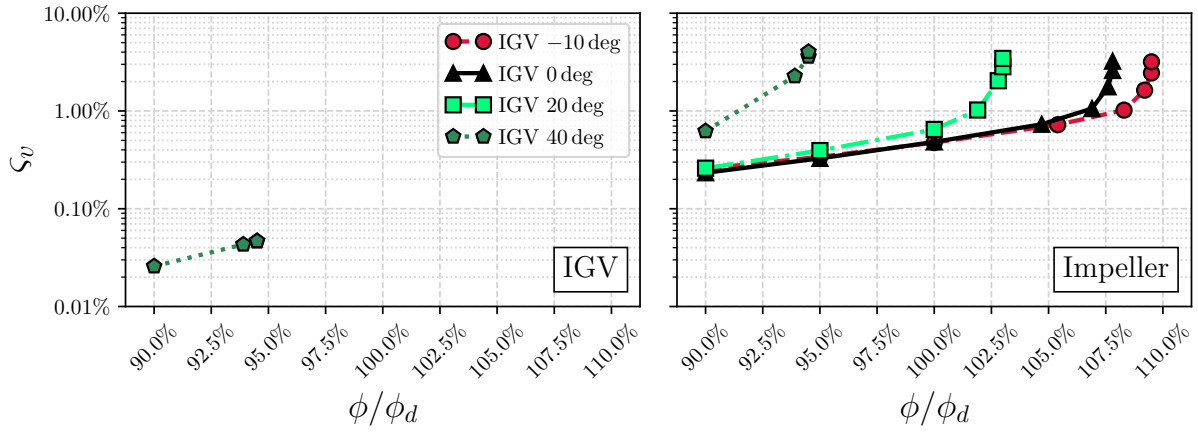


Figure 12: Normalized vapor mass in the IGV and impeller domain. The vapor phase appears in the IGV domain only for vane rotation of 40 deg.

choking (nearly constant for all preswirls). As commented earlier, the vapor mass fraction at a constant flow rate is always higher for positive preswirls.

As the computational model describes the two-phase properties in terms of mass or volume averages, the entropy production and local interactions between the two phases are neglected. Nonetheless, the occurrence of two-phase flows has a direct effect on the compressor characteristic curves by establishing the choking limit. Figure 13 reports the flow field in terms of Mach number (relative or absolute depending on the component) and the field of vapor mass fraction along the blade-to-blade plane at midspan for different inlet vane rotations at the choked flow rate. For all cases, the region of high Mach number can be associated with the presence of two-phase flows. This is a consequence of the abrupt reduction in speed of sound of the two-phase mixture compared to the single-phase counterpart when the secondary phase is lighter than the primary one (cavitation phenomenon) [15]. It is worth highlighting that the maximum Mach number outside the two-phase region is close to 0.5, i.e., there is a subsonic flow regime that would lead choking at considerably higher flow rates. Here, the choking occurs when the two-phase region occupies the entire throat. Such peculiar effect of two-phase flows on compressor characteristic curve has been also experimentally verified by Toni *et al.* [32]. As the negative prerotation reduces the incidence at high flow rates, the available area for the flow increases thanks to a reduced blockage, and the choking limit shifts to higher flow rates accordingly.

## 6. Concluding remarks

This work has examined the performance of a representative centrifugal compressor for power systems that operates $CO_2$ close to the critical point (upstream conditions: $P = 78.70\,\text{bar}$, $T = 305.15\,\text{K}$) by means of steady RANS simulations. Besides the impeller, the computational domain includes adjustable inlet guide vanes and a wedge-shaped vaned diffuser. The computational model features a state-of-the-art equation of state supplied in

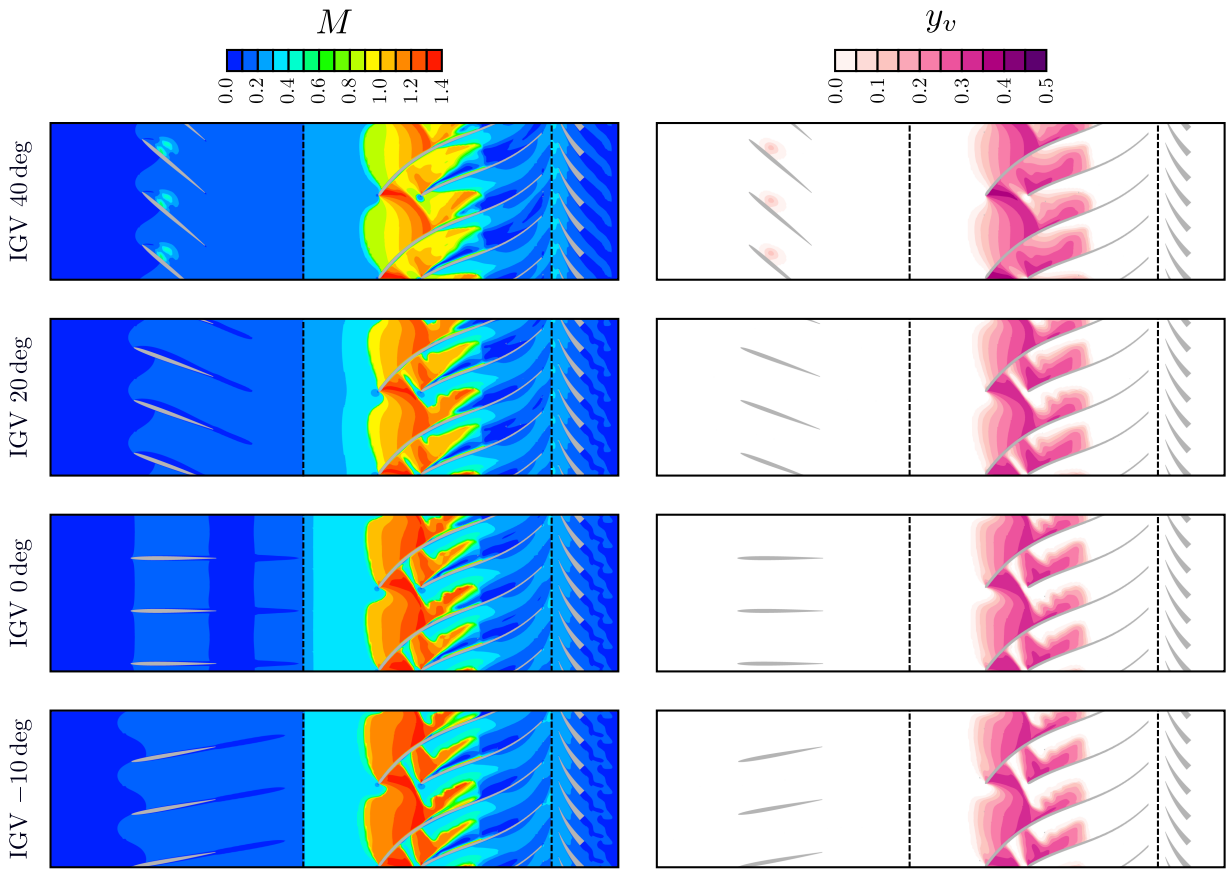


Figure 13: Mach number and vapor mass fraction fields on the blade-to-blade plane at midspan for different vane rotations at choking. Black dashed lines indicate the mixing planes.

tabular forms and describes the two-phase flows in terms of averaged mixture properties at thermodynamic equilibrium. It is found that:

- A single-stage centrifugal compressor can deliver the entire pressure ratio required by the thermodynamic cycle ($\sim 3.25$) in an efficient way ($\eta = 87.9\%$, excluding parasitic losses). It is noted, however, that such high value benefits from the large scale of the machine, and smaller values are expected for power plants with rated power smaller than 50 MW.

- A loss decomposition shows that the vaned diffuser generates 7.5% of dissipation at design conditions, while the loss in the impeller is 4.5%. The IGV loss is negligible (maximum 0.2%) by rotating vanes between $-10$ deg and 20 deg but raises to 1.0% for 40 deg rotation due to significant flow separation.

- The flow range with no preswirl is included between 90.0% and 107.8%. The choking limit increases up to 109.5% with a negative preswirl of $-10$ deg. The left limit is numerically determined by flow separation in the vaned diffuser, which prevents achieving

a steady solution. The IGV has no perceivable effects on the vaned diffuser, hence the left limit does not change with preswirl. Therefore, it could be a better solution to opt for a vaneless diffuser over a vaned configuration to improve compressor flexibility under IGV regulation.

- The choking limit is set by the occurrence of two-phase flow in the impeller intake region. This evidence stresses the importance of two-phase effects on the overall compressor operation and poses specific challenges to the aerodynamic design of the impeller to minimize such effects. An additional alternative to reduce the aerodynamic loading on the impeller with positive effects on the two-phase onset could be to split the compression process in more stages.

- Positive prerotation inducing a negative incidence on the impeller blades promotes the occurrence of a two-phase flow therein because the flow accelerates to recover the blade angle direction.

- In all cases analyzed, the vaned diffuser never faced two-phase flows. Furthermore, the IGV produced a localized two-phase region ($< 0.10\%$ in volume) only for vane rotation 40 deg. Considering that the studied compressor arguably exacerbates the onset of two-phase flow due to the combination of near-critical conditions and high aerodynamic loading, standard criteria can be confidently adopted for the design and analysis of these two components.

## Appendix A. Reynolds-averaged enthalpy-based energy equation

The steady-state energy equation expressed in terms of specific enthalpy reads as:

$$\partial_i \left(\rho v_i h\right) = \partial_i \left(\kappa\, \partial_i T\right) + v_i\, \partial_i P + \tau_{ij}\, \partial_i v_j \tag{A.1}$$

where $\tau_{ij} = \mu\left(\left[\partial_j v_i + \partial_i v_j\right] - 2/3\, \partial_k v_k \delta_{ij}\right)$. The indices follow the Einstein summation convention. $\partial_i(\cdot)$ is a shorthand for $\partial(\cdot)/\partial x_i$.

The gross effect of turbulence is included by considering the corresponding Reynolds-averaged equation. To obtain this equation, density and pressure are decomposed into a mean and a fluctuating part, i.e. $\psi = \overline{\psi} + \psi'$ (Reynolds decomposition), while the other quantities are expressed following the Favre decomposition, $\psi = \widetilde{\psi} + \psi''$, where $\widetilde{\psi} = \overline{\rho\psi}/\overline{\rho}$ is the mass-averaged value and $\psi'' = -\overline{\rho'\psi'}/\overline{\rho}$ includes the density fluctuation in the property fluctuation. Finally, turbulent fluctuations in transport properties are customary neglected. By plugging the above decompositions in (A.1) and, then, taking the Reynolds average, the Reynolds-averaged enthalpy-based energy equation is obtained:

$$\begin{aligned}\partial_i \left(\overline{\rho}\widetilde{v_i}\widetilde{h} + \overline{\rho v_i'' h''}\right) = {} & \partial_i \left(\kappa\, \partial_i \widetilde{T}\right) + \partial_i \left(\kappa\, \partial_i \overline{T''}\right) + \widetilde{v_i}\, \partial_i \overline{P} + \overline{v_i''}\, \partial_i \overline{P} \\ & + \overline{v_i''\, \partial_i P'} + \widetilde{\tau_{ij}}\, \partial_i \widetilde{v_j} + \overline{\tau_{ij}''\, \partial_i v_j''} + \overline{\tau_{ij}''}\, \partial_i \widetilde{v_j} + \widetilde{\tau_{ij}}\, \partial_i \overline{v_j''}\end{aligned} \tag{A.2}$$

Fluctuating terms that arise from the Reynolds and Favre decomposition have to be modelled. In this work, we only model the turbulent diffusion and the increase of thermal energy due to turbulent kinetic energy (TKE) dissipation. Other terms are neglected because of the lack of reliable closure models. The turbulent diffusion is modelled on the basis of the Reynolds analogy, while the dissipation of TKE is closely linked with the employed turbulence model, and they read respectively as:

$$\overline{\rho v_i'' h''} = -\frac{\mu_T}{Pr_T}\partial_i \widetilde{h} \tag{A.3}$$

$$\overline{\tau_{ij}'' \, \partial_i v_j''} = \overline{\rho}\varepsilon \tag{A.4}$$

where $\varepsilon = \beta^* k\omega$, with $\beta^* = 0.09$, in accordance with the $k-\omega$ SST turbulence model. The turbulent Prandtl number $Pr_T$ is modelled according to the conduction model proposed by Kays and Crawford [23, eq. 13-7]:

$$Pr_T = \frac{1}{\dfrac{1}{2Pr_{T\infty}} + C^* \, Pe_T \sqrt{\dfrac{1}{Pr_{T\infty}}} - (C^* \, Pe_T)^2 \left[1 - \exp\left(-\dfrac{1}{C^* \, Pe_T \sqrt{Pr_{T\infty}}}\right)\right]} \tag{A.5}$$

where $Pr_{T\infty} = 0.85$, $C^* = 0.3$, and $Pe_T = \mu_T \, c_P/\kappa$.

Note that Smolka *et al.* [22] assume local equilibrium between production and dissipation of TKE, therefore they model the irreversible degradation of TKE into thermal energy as $\widetilde{\tau_{Tij}}\partial_i \widetilde{v_j}$ with $\widetilde{\tau_{Tij}} = \mu_T \left([\partial_j \widetilde{v_i} + \partial_i \widetilde{v_j}] - 2/3 \, \partial_k v_k \delta_{ij}\right) - 2/3 \rho k \delta_{ij}$. However, this equilibrium condition is usually not entirely recovered in boundary layers with adverse pressure gradient, such as those developing in compressors [37].

## Appendix B. Mixed-out state with an arbitrary equation of state

The mixed-out state is the corresponding state of complete equilibrium (mechanical and thermal) associated with an initial state in non-equilibrium. This reference state is introduced to account for all the cumulative losses that are inherently possessed by a non-uniform flow. As a matter of fact, a non-uniform flow produces entropy while mixing to achieve equilibrium condition. This means that blade performance estimates are sensitive to the specific measurement location as long as the flow is not entirely mixed out. To overcome this problem, it is convenient to refer the blade performance to the mixed-out state. In this way, the mixing loss is entirely ascribed to the component that generates the non-uniform flow in the first place.

This appendix extends for an arbitrary thermodynamic model the procedure illustrated by Prasad [38]. Two separate cases are discussed: swirling flows in annular geometry (e.g., at the outlet of the inlet guide vane) and swirling flows in cylindrical geometry (e.g., at the outlet of the impeller and vaned diffuser).

The mixed-out state for swirling flows in annular geometry (with internal radius $R_i$, external radius $R_e$, and circumferential extent $\Theta = 2\pi/N_{blade}$) is characterized by (i) axial

invariance, (ii) circumferential uniformity, (iii) thermal equilibrium, and (iv) radial equilibrium. To satisfy these hypotheses it is required that $v_{ax} = C_{ax}$, $v_\theta(r) = C_\theta\, r$, $T = C_T$, and $P = P(r)$ complying with the radial equilibrium, where $C_{ax}$, $C_\theta$, and $C_T$ are constants to be determined. Continuity, axial momentum, angular momentum, and total energy are conserved from the initial measurement plane to the mixed-out state. Therefore, the mixed-out state can be determined by solving the following system of equations:

$$\dot{m} = \Theta\, C_{ax} \int_{R_i}^{R_e} \rho r\, dr \tag{B.1a}$$

$$\dot{m}\widetilde{v_{ax}} + \overline{P}A = \Theta\, C_{ax}^2 \int_{R_i}^{R_e} \rho r\, dr + \Theta \int_{R_i}^{R_e} Pr\, dr \tag{B.1b}$$

$$\dot{m}r\widetilde{v_\theta} = \Theta\, C_{ax}\, C_\theta \int_{R_i}^{R_e} \rho r^3\, dr \tag{B.1c}$$

$$\dot{m}\left(\widetilde{h} + 0.5\widetilde{v^2}\right) = \Theta\, C_{ax} \int_{R_i}^{R_e} \rho h r\, dr + 0.5\,\Theta\, C_{ax}^3 \int_{R_i}^{R_e} \rho r dr + 0.5\,\Theta\, C_{ax}\, C_\theta^2 \int_{R_i}^{R_e} \rho r^3 dr \tag{B.1d}$$

The left-hand sides of system (B.1) refer to the measurement plane, and they can be immediately evaluated by extracting the mass flow rate ($\dot{m}$) and the indicated mass-flow ($\widetilde{v_{ax}}, \widetilde{rv_\theta}, \widetilde{h}, \widetilde{v^2}$) and area ($\overline{P}$) averages from the CFD solution. The right-hand sides of system (B.1) include the corresponding mixed-out quantities. The radial evolution of thermodynamic properties is strictly linked with the hypothesis of radial equilibrium, i.e., the radial gradient of pressure has to balance the centrifugal stress:

$$\frac{\partial P}{\partial r} = \rho C_\theta^2 r \tag{B.2}$$

In the above expressions, the density is related to pressure (variable along the radius) and temperature (constant) via the thermal equation of state, $\rho = \mathcal{D}(P(r), C_T)$. Similarly, the static enthalpy in equation (B.1d) is linked to pressure and temperature as $h = \mathcal{H}(P(r), C_T)$. The thermodynamic functions $\mathcal{D}$ and $\mathcal{H}$ that relate density and static enthalpy, respectively, to the indicated state variables are computed via CoolProp. The lack of an explicit function for $\mathcal{D}$ and $\mathcal{H}$ implies to solve the integrals in (B.1) numerically.

The numerical strategy used in this work to solve eq. (B.1) is described as follows. $C_{ax}$, $C_\theta$, $C_T$, and $P(r = R_i)$ are selected as independent variables of the system of equations (B.1). The system is solved with `fsolve` available in `scipy` module using the average values from the CFD solution as initial conditions and $1 \times 10^{-6}$ as convergence criterion. The integrals are evaluated with the trapezoidal rule using 200 points to discretize the radial coordinate. This radial discretization is found sufficiently accurate to estimate radial-averaged performance estimates with a negligible error (less than 0.1%). The radial evolution of thermodynamic properties is obtained by solving the ordinary differential equation (B.2) with first-order finite difference. Notice that equation (B.2) must be solved iteratively because of the dependence of $\rho$ on pressure and temperature. The convergence criterion for (B.2) is $L^\infty(P)$-error smaller than $1 \times 10^{-6}$.

The mixed-out state for swirling flows in cylindrical geometry (with radius $R$, width $b$, and circumferential extent $\Theta = 2\pi/N_{blade}$) is easier to be determined than in annular geometry as thermodynamic properties and velocity components are uniform over the mixed-out plane. Moreover, as the axial component of velocity is negligible, its value is set to zero and the axial momentum equation is not included in the system of equations. Therefore, the mixed-out state is obtained by requiring $v_r = C_r$, $v_\theta = C_\theta$, $T = C_T$, and $P = C_P$, where $C_r$, $C_\theta$, $C_T$, and $C_P$ are constants to be determined. The system of equations reads as:

$$\dot{m} = \rho\, C_r\, \Theta R b \tag{B.3a}$$

$$\dot{m}\widetilde{v_r} + \overline{P}A = \rho\, C_r^2\, \Theta R b + C_P\, \Theta R b \tag{B.3b}$$

$$\dot{m}\widetilde{v_\theta} = \rho\, C_r\, C_\theta\, \Theta R b \tag{B.3c}$$

$$\dot{m}\left(\widetilde{h} + 0.5\widetilde{v^2}\right) = \rho\, C_r\, \Theta R b\, \left(h + 0.5(C_r^2 + C_\theta^2)\right) \tag{B.3d}$$

where $\rho = \mathcal{D}(C_P, C_T)$ and $h = \mathcal{H}(C_P, C_T)$. Note that any pair of state variables can be equivalently selected in place of pressure and temperature to solve the system of equations, as all thermodynamic properties are uniform over the mixed-out plane. As there are no integrals nor ordinary differential equations to be approximated, the numerical problem only involves finding the roots of a system of non-linear equations. In this work, the system (B.3) is solved with `fsolve` from `scipy` module using the average values from the CFD solution as initial conditions and $1 \times 10^{-6}$ as convergence criterion.

## Nomenclature

### Roman letter

| | |
|---|---|
| $A$ | area |
| $b$ | channel height |
| $b_2$ | blade height at impeller outlet, 11.5 mm |
| $C_{ax}, C_\theta, C_r$ | constants for mixed-out procedure |
| $C_T, C_P$ | constants for mixed-out procedure |
| $C^*$ | constant, 0.3 |
| $c$ | speed of sound |
| $c_P$ | specific heat at constant pressure |
| $\mathcal{D}$ | thermodynamic functions for $\rho$ |
| $e_a$ | approximate relative error |
| $e_{ext}$ | extended relative error |
| $h$ | specific enthalpy |
| $\mathcal{H}$ | thermodynamic functions for $h$ |
| $k$ | turbulent kinetic energy |
| $\mathcal{K}$ | thermodynamic functions for $\kappa$ |
| $l$ | eulerian work |
| $l_{is}$ | isentropic work |

| | |
|---|---|
| $M$ | Mach number |
| $M_{u2}$ | peripheral Mach number, $u_2/c_0$ |
| $\dot{m}$ | mass flow rate |
| $N_{blade}$ | blade number |
| $P$ | pressure |
| $\mathcal{P}$ | thermodynamic functions for $P$ |
| $Pe_T$ | turbulent Peclet number |
| $Pr_T$ | turbulent Prandtl number |
| $Pr_{T\infty}$ | free-stream turbulent Prandtl number, 0.85 |
| $R$ | radius |
| $R_i$ | internal (hub) radius |
| $R_e$ | external (tip) radius |
| $Re_{u2}$ | peripheral Reynolds number, $\rho u_2 b_2/\mu_0$ |
| $r$ | radial coordinate |
| $s$ | specific entropy |
| $T$ | temperature |
| $u$ | peripheral velocity |
| $u_2$ | peripheral velocity at impeller outlet, 204.20 m/s |
| $v$ | absolute velocity |
| $v_{ax}$ | axial component of absolute velocity |
| $v_\theta$ | tangential component of absolute velocity |
| $v_r$ | radial component of absolute velocity |
| $w$ | relative velocity |
| $\mathcal{X}$ | thermodynamic functions for $y_v$ |
| $y_v$ | vapor mass fraction |
| $z$ | axial coordinate |

**Greek letter**

| | |
|---|---|
| $\alpha_v$ | vapor volume fraction |
| $\beta^*$ | constant, 0.09 |
| $\delta_{ij}$ | Kronecker delta |
| $\Delta\eta_i$ | IGV loss |
| $\Delta\eta_r$ | impeller loss |
| $\Delta\eta_d$ | vaned diffuser loss |
| $\varepsilon$ | rate of dissipation of turbulent kinetic energy |
| $\eta$ | total-total efficiency |
| $\theta$ | area circumferential extent |
| $\kappa$ | thermal conductivity |
| $\lambda$ | work coefficient |
| $\mu$ | dynamic viscosity |
| $\mu_T$ | eddy viscosity |
| $\Pi$ | total-total pressure ratio |
| $\rho$ | (mixture) density |

| | |
|---|---|
| $\rho_v$ | vapor density |
| $\varsigma_v$ | integral vapor mass fraction |
| $\tau$ | viscous stress tensor |
| $\tau_T$ | Reynolds stress tensor |
| $\phi$ | flow coefficient, $\dot{m}/(\rho u_2 D_2^2)$ |
| $\omega$ | rotational speed, turbulence frequency |

**Superscripts & Subscripts**

| | |
|---|---|
| $(\cdot)_c$ | at critical point |
| $(\cdot)_d$ | at design point |
| $(\cdot)_{ref}$ | reference state |
| $(\cdot)^t$ | total quantity |
| $(\cdot)_0$ | intake total state |
| $(\cdot)_1$ | at $z = -75.0\,\mathrm{mm}$ |
| $(\cdot)_{\hat{1}}$ | mixed-out state from $z = -75.0\,\mathrm{mm}$ |
| $(\cdot)_2$ | at $r = 214.0\,\mathrm{mm}$ |
| $(\cdot)_{\hat{2}}$ | mixed-out state from $r = 214.0\,\mathrm{mm}$ |
| $(\cdot)_3$ | at $r = 317.3\,\mathrm{mm}$ |
| $(\cdot)_{\hat{3}}$ | mixed-out state from $r = 317.3\,\mathrm{mm}$ |
| $\overline{(\cdot)}$ | Reynolds averaged (app. A), area averaged (app. B) |
| $\widetilde{(\cdot)}$ | Favre averaged (app. A), mass-flow averaged (app. B) |
| $(\cdot)'$ | Reynolds fluctuation |
| $(\cdot)''$ | Favre fluctuation |
| $(\cdot)^{(i)}$ | i-grid solution (i = 1: fine, 2: medium, 3: coarse) |

**Acronym**

| | |
|---|---|
| CFD | computational fluid dynamic |
| EOS | equation of state |
| GCI | grid convergence index |
| HEM | homogeneous equilibrium model |
| IGV | inlet guide vane |
| LUT | look-up tables |
| RANS | Reynolds-averaged Navier-Stokes |
| $sCO_2$ | supercritical carbon dioxide |
| SNL | Sandia National Laboratories |
| TKE | turbulent kinetic energy |
| UDF | user-defined function |
| UDS | user-defined scalar |

## References

[1] M.-J. Li, J.-L. Xu, F. Cao, J.-Q. Guo, Z.-X. Tong, H.-H. Zhu, The investigation of thermo-economic performance and conceptual design for the miniaturized lead-cooled fast reactor composing supercritical co2 power cycle, Energy 173 (2019) 174–195. doi:10.1016/j.energy.2019.01.135.

[2] D. Thanganadar, F. Fornarelli, S. Camporeale, F. Asfand, J. Gillard, K. Patchigolla, Thermo-economic analysis, optimisation and systematic integration of supercritical carbon dioxide cycle with sensible heat thermal energy storage for csp application, Energy 238 (2022) 121755. doi:10.1016/j.energy.2021.121755.
[3] D. Alfani, M. Binotti, E. Macchi, P. Silva, M. Astolfi, sCO2 power plants for waste heat recovery: design optimization and part-load operation strategies, Applied Thermal Engineering 195 (2021) 117013. doi:10.1016/j.applthermaleng.2021.117013.
[4] G. Musgrove, S. Wright, 1 - Introduction and background, in: K. Brun, P. Friedman, R. Dennis (Eds.), Fundamentals and Applications of Supercritical Carbon Dioxide ($sCO_2$) Based Power Cycles, Woodhead Publishing, 2017, pp. 1 – 22. doi:10.1016/B978-0-08-100804-1.00001-3.
[5] D. Alfani, M. Astolfi, M. Binotti, P. Silva, Part-Load Strategy Definition and Preliminary Annual Simulation for Small Size sCO2-Based Pulverized Coal Power Plant, Journal of Engineering for Gas Turbines and Power 143 (9), 091026 (08 2021). doi:10.1115/1.4051003.
[6] C. Lettieri, D. Yang, Z. Spakovszky, An Investigation of Condensation Effects in Supercritical Carbon Dioxide Compressors, Journal of Engineering for Gas Turbines and Power 137 (8) (08 2015). doi:10.1115/1.4029577.
[7] N. D. Baltadjiev, C. Lettieri, Z. S. Spakovszky, An Investigation of Real Gas Effects in Supercritical CO2 Centrifugal Compressors, Journal of Turbomachinery 137 (9) (09 2015). doi:10.1115/1.4029616.
[8] A. Ameli, A. Afzalifar, T. Turunen-Saaresti, J. Backman, Centrifugal Compressor Design for Near-Critical Point Applications, Journal of Engineering for Gas Turbines and Power 141 (3) (2018). doi:10.1115/1.4040691.
[9] A. Romei, P. Gaetani, A. Giostri, G. Persico, The role of turbomachinery performance in the optimization of supercritical carbon dioxide power systems, Journal of Turbomachinery 142 (7) (2020) 071001. doi:10.1115/1.4046182.
[10] S. K. Cho, S. Son, J. Lee, S.-W. Lee, Y. Jeong, B. S. Oh, J. I. Lee, Optimum loss models for performance prediction of supercritical co2 centrifugal compressor, Applied Thermal Engineering 184 (2021) 116255. doi:10.1016/j.applthermaleng.2020.116255.
[11] R. Pecnik, E. Rinaldi, P. Colonna, Computational Fluid Dynamics of a Radial Compressor Operating With Supercritical CO2, Journal of Engineering for Gas Turbines and Power 134 (12) (10 2012). doi:10.1115/1.4007196.
[12] F. Moraga, D. Hofer, S. Saxena, R. Mallina, Numerical Approach for Real Gas Simulations: Part I Tabular fluid properties for real gas analysis, in: Proceedings of the ASME Turbo Expo 2017, 2017, pp. 1–8, paper no. GT2017-63148. doi:10.1115/GT2017-63148.
[13] A. Hosangadi, Z. Liu, T. Weathers, V. Ahuja, J. Busby, Modeling Multiphase Effects in $CO_2$ Compressors at Subcritical Inlet Conditions, Journal of Engineering for Gas Turbines and Power 141 (8) (2019) 081005. doi:10.1115/1.4042975.
[14] M. Palacz, J. Smolka, A. Fic, Z. Bulinski, A. J. Nowak, K. Banasiak, A. Hafner, Application range of the HEM approach for CO2 expansion inside two-phase ejectors for supermarket refrigeration systems, International Journal of Refrigeration 59 (2015) 251 – 258. doi:10.1016/j.ijrefrig.2015.07.006.
[15] A. Romei, G. Persico, Computational fluid-dynamic modelling of two-phase compressible flows of carbon dioxide in supercritical conditions, Applied Thermal Engineering 190 (2021) 116816. doi:10.1016/j.applthermaleng.2021.116816.
[16] H. Pham, N. Alpy, J. Ferrasse, O. Boutin, M. Tothill, J. Quenaut, O. Gastaldi, T. Cadiou, M. Saez, An approach for establishing the performance maps of the sc-CO2 compressor: Development and qualification by means of CFD simulations, International Journal of Heat and Fluid Flow 61 (2016) 379–394. doi:10.1016/j.ijheatfluidflow.2016.05.017.
[17] A. Ameli, T. Turunen-Saaresti, J. Backman, Numerical Investigation of the Flow Behavior Inside a Supercritical CO2 Centrifugal Compressor, Journal of Engineering for Gas Turbines and Power 140 (12) (2018). doi:10.1115/1.4040577.
[18] W. Shao, J. Yang, X. Wang, Z. Ma, Accuracy study and stability control of a property-table-based cfd strategy for modeling sco2 compressors working near the critical point of the fluid, Applied Thermal Engineering 183 (2021) 116222. doi:10.1016/j.applthermaleng.2020.116222.

[19] S. A. Wright, R. F. Radel, M. E. Vernon, G. E. Rochau, P. S. Pickard, Operation and analysis of a supercritical $CO_2$ Brayton cycle, Sandia Report SAND2010-0171 (2010).
[20] S. Saxena, R. Mallina, F. Moraga, D. Hofer, Numerical Approach for Real Gas Simulations: Part II Flow Simulation for Supercritical CO2 Centrifugal Compressor, in: Proceedings of the ASME Turbo Expo 2017, 2017, pp. 1–12, paper no. GT2017-63149. doi:10.1115/GT2017-63149.
[21] G. Persico, P. Gaetani, A. Romei, L. Toni, E. F. Bellobuono, R. Valente, Implications of Phase Change on the Aerodynamics of Centrifugal Compressors for Supercritical Carbon Dioxide Applications, Journal of Engineering for Gas Turbines and Power 143 (4) (2021). doi:10.1115/1.4049924.
[22] J. Smolka, Z. Bulinski, A. Fic, A. Nowak, K. Banasiak, A. Hafner, A computational model of a transcritical R744 ejector based on a homogeneous real fluid approach, Applied Mathematical Modelling 37 (3) (2013) 1208–1224. doi:10.1016/j.apm.2012.03.044.
[23] W. Kays, M. Crawford, Convective Heat and Mass Transfer (3rd edition), McGraw-Hill, New York, 1993.
[24] F. Menter, Two-equation eddy-viscosity turbulence models for engineering applications, AIAA Journal 32 (8) (1994) 1598–1605. doi:10.2514/3.12149.
[25] P. Smirnov, F. Menter, Sensitization of the SST turbulence model to rotation and curvature by applying the spalart-shur correction term, Journal of Turbomachinery 131 (4) (2009) 1–8. doi:10.1115/1.3070573.
[26] T. Barth, D. Jespersen, The design and application of upwind schemes on unstructured meshes, in: AIAA 27th Aerospace Sciences Meeting, 1989, pp. 1–12. doi:10.2514/6.1989-366.
[27] I. H. Bell, J. Wronski, S. Quoilin, V. Lemort, Pure and pseudo-pure fluid thermophysical property evaluation and the open-source thermophysical property library coolprop, Industrial & Engineering Chemistry Research 53 (6) (2014) 2498–2508. doi:10.1021/ie4033999.
[28] R. Span, W. Wagner, A new equation of state for carbon dioxide covering the fluid region from the triple-point temperature to 1100 K at pressures up to 800 MPa, Journal of Physical and Chemical Reference Data 25 (6) (1996) 1509–1596. doi:10.1063/1.555991.
[29] A. Fenghour, W. Wakeham, V. Vesovic, The viscosity of carbon dioxide, Journal of Physical and Chemical Reference Data 27 (1) (1998) 31–39. doi:10.1063/1.556013.
[30] G. Scalabrin, P. Marchi, F. Finezzo, R. Span, A reference multiparameter thermal conductivity equation for carbon dioxide with an optimized functional form, Journal of Physical and Chemical Reference Data 35 (4) (2006) 1549–1575. doi:10.1063/1.2213631.
[31] M. Nakagawa, M. S. Berana, A. Kishine, Supersonic two-phase flow of co2 through convergingdiverging nozzles for the ejector refrigeration cycle, International Journal of Refrigeration 32 (6) (2009) 1195–1202. doi:https://doi.org/10.1016/j.ijrefrig.2009.01.015.
[32] L. Toni, F. E. Bellobuono, R. Valente, A. Romei, P. Gaetani, G. Persico, Experimental and Numerical Performance Survey of a MW-Scale Supercritical CO2 Compressor Operating in Near-Critical Conditions, in: The 7th International Supercritical CO2 Power Cycle Symposium, 2022, pp. 1–16, paper no. 177.
[33] A. Whitfield, N. C. Baines, Design of radial turbomachines, Longman Singapore Publishers Ltd., 1990.
[34] R. Van den Braembussche, Design and Analysis of Centrifugal Compressors, ASME Press and John Wiley & Sons Ltd, 2019.
[35] I. Celik, U. Ghia, P. Roache, C. Freitas, H. Coleman, P. Raad, Procedure for Estimation and Reporting of Uncertainty Due to Discretization in CFD Applications, Journal of Fluids Engineering 130 (7) (2008). doi:10.1115/1.2960953.
[36] M. Casey, C. Robinson, Radial Flow Turbocompressors: Design, Analysis, and Applications, Cambridge University Press, 2021. doi:10.1017/9781108241663.
[37] A. Wheeler, A. Dickens, R. Miller, The effect of nonequilibrium boundary layers on compressor performance, Journal of Turbomachinery 140 (10) (2018) 101003. doi:10.1115/1.4040094.
[38] A. Prasad, Calculation of the Mixed-Out State in Turbomachine Flows, Journal of Turbomachinery 127 (3) (2004) 564–572. doi:10.1115/1.1928289.